A Planning and Guidance Platform for Cardiac Resynchronization Therapy

Peter Mountney, Jonathan M. Behar, Daniel Toth, Maria Panayiotou, Sabrina Reiml, Marie-Pierre Jolly, Rashed Karim, Li Zhang, Alexander Brost, Christopher A. Rinaldi, Kawal Rhode

***Abstract*—Patients with drug-refractory heart failure can greatly benefit from cardiac resynchronization therapy (CRT). A CRT device can resynchronize the contractions of the left ventricle (LV) leading to reduced mortality. Unfortunately 30-50 % of patients do not respond to treatment when assessed by objective criteria such as cardiac remodeling. A significant contributing factor is suboptimal placement of the LV lead. It has been shown that placing this lead away from scar and at the point of latest mechanical activation can improve response rates. This paper presents a comprehensive and highly automated system that uses scar and mechanical activation to plan and guide CRT procedures. Standard clinical preoperative magnetic resonance imaging is used to extract scar and mechanical activation information. The data is registered to a single 3D coordinate system and visualized in novel 3D and 2D American Heart Association plots enabling the clinician to select target segments. During the procedure, the planning information is overlaid onto live fluoroscopic images to guide lead deployment. The proposed platform has been used during 14 CRT procedures and validated on synthetic, phantom, volunteer and patient data.**

I. Introduction

CARDIOVASCULAR disease is the leading global cause of death, it accounts for over 30 % of deaths per year and is expected to rise to over 23.6 million per year by 2030 [1]. In the past 25 years, cardiac resynchronization therapy (CRT) has been one of the most successful therapies to emerge for patients with advanced drug-refractory heart failure (HF), systolic dysfunction and ventricular dyssynchrony. Unfortunately, 30-50 % of the patients do not respond to this therapy when assessed by objective criteria such as cardiac remodeling [2].

CRT aims to resynchronize the contractions of the heart's ventricles by implanting a device which delivers pacing electrical signals into the myocardial tissue. The device is connected to three pacing leads which are placed in the right atrium, right ventricle (RV) and left ventricle (LV). The LV lead is typically placed through the coronary sinus (CS) and into the coronary vein on the epicardial surface under intra-operative fluoroscopic guidance. The location of the LV lead is critical to successful cardiac resynchronization and sub-optimal lead placement can lead to non-response.

Peter Mountney, Marie-Pierre Jolly & Li Zhang - Medical Imaging Technologies, Siemens Healthineers, USA

Daniel Toth is with Siemens Healthineers Ltd, United Kingdom

Maria Panayiotou, Daniel Toth, Rashed Karim & Kawal Rhode - Division of Imaging Sciences and Biomedical Engineering, Kings College London, UK

Sabrina Reiml & Alexander Brost - Siemens Healthineers GmbH, Germany

Jonathan M. Behar and Christopher A. Rinaldi - Department of Cardiology, Guy's and St. Thomas' NHS Foundation Trust

Determining the optimal LV placement is an area of significant research. There are several factors affecting it.

- Anatomical position: Studies [3], [4] have shown that lateral, anterior, or posterior LV lead locations have the best responses. Apical LV lead placement is considered suboptimal due to its proximity to the RV lead [5].
- Coronary venous anatomy: The structure of the vessel branches limits the target locations on the LV epicardium surface. Additionally, the vessel must be wide enough to allow the lead to pass through it and sufficiently structured to eable the lead to be securely lodged.
- Scar: Pacing in tissue with scar is associated with ineffective capture, slow conduction or blockage and less heamodynamic improvement [6]. Placing the lead away from scar tissue resulted in a better clinical outcome [7].
- Mechanical activation: It has been shown [8], [9] that pacing sites with the greatest mechanical delay results in improved clinical outcomes and greater LV remodeling.
- Phrenic nerve stimulation (PNS): PNS during the implant may require the lead to be placed at a more basal site which has higher risk of lead dislodgement.

The retrospective and prospective clinical studies described above have demonstrated that response rates can be improved. With current clinical approaches, the CS anatomy can be visualized with contrast injected venograms and PNS detected during implantation. However, deriving scar and mechanical activation information requires additional imaging modalities and significant image processing. The information is inherently complex and needs to be visualized in a simple and intuitive manner, to enable effective planning and guidance.

A. Literature Review

The nature of the problems outlined above and the complexity of the pipeline required for CRT planning and guidance means translating a comprehensive system to the operating room is challenging. Several approaches have been proposed for planning and guidance [10]–[12] or retrospective data fusion for offline visualization [13], [14]. This section compares these approaches by their constituent components: 1) preoperative imaging modality, 2) intramodality registration, 3) segmentation, 4) visualization of planning data, 5) guidance.

It is currently not possible to obtain all the required information for planning and guiding a CRT procedure from a single imaging modality in a single acquisition. A number of approaches have been proposed which use single modality

with multiple acquisitions or multiple modalities. Single-photon emission computed tomography (SPECT) imaging has a been used to extract myocardial perfusion [12] and infer scar location, however, it is not possible to separate this from ischemic tissue or compute mechanical or electrical activation. Multiple magnetic resonance imaging (MRI) acquisitions (cine, late gadolinium enhancement (LGE) and whole heart) have been used to extract mechanical activation, scar and the CS location [10], [11], although whole heart MRI imaging of heart failure patients is challenging given the duration of current acquisitions and breath holds requirements. Two studies [13], [14] combine ultrasound (US), computed tomography (CT) and electro-anatomical maps (EAM). Combining multiple acquisitions or modalities requires the images to be registered so that data can be analyzed in the same coordinate system.

Registering multiple preoperative modalities or acquisitions is a fundamental component of data fusion. A system using MRI [10], [11] aligns the coordinate systems of the LGE and whole heart imaging using the dicom image origins. No image-based registration is performed between acquisitions to account for differences due to patient shift, respiration and cardiac phase. Furthermore mechanical activation is computed by processing the cine images using 3rd party software in an undefined coordinate system. EAM and US data to CT [13] registration has been proposed using a semi-automated and automated approach respectively, however it should be noted that EAM is generally considered to be intraoperative data.

Anatomy segmentation methods are modality specific. A LV epicardial model based approach is proposed using whole heart MRI [10], [11] with manual CS segmentation using ITKSnap. A semi automated [12] approach is used to extract the myocardium and infer the epicardial wall from single phase SPECT, however segmentation accuracy is limited by the 6.4 mm voxel size. In CT, the LV endocardium can be segmented [13] using a semi automated fuzzy connectedness algorithm.

Automatic scar segmentation for CRT has been proposed [10], [11], however, this is sensitive to image quality and defaults to a manual approach. Other approaches [12], [13] do not explicitly segment scar.

It is challenging to visualize complex data from multiple sources in a simple and intuitive way. Segmented data such as scar, LV or CS can be visualized in 3D [10]–[12], [14], however current approaches do not incorporate scar transmurality or mechanical activation. An alternative approach to link the data together uses the 16 segment American Heart Association (AHA) model to show scar distribution and CS [10], [11]. This abstract coordinate system is well suited to planning, but it is far removed from the procedure coordinate system making, it challenging to use during guidance.

For guidance, the 3D planning data can be visualized side by side with intraoperative fluoroscopy [12], [14]. The two coordinate systems are not linked and the clinician must make a mental alignment of the data. Registering the preoperative data to the intraoperative fluoroscopic images [10], [11], [15] provides more intuitive image guided overlay; however, cross modality MR to X-ray registration remains challenging.

B. Contribution

There is a real clinical need for a planning and guidance platform for CRT. Ad hoc prototypes and retrospective studies have shown that response rates can be improved, however, to push this science forward, impact the clinical community, impact patients and inform future medical imaging research, a comprehensive platform is required.

The level of impact that this science will have on changing the landscape of CRT is highly dependent on 1) how easily it can fit to the current clinical workflow and be adopted, 2) how automated the system can be made, 3) how quickly clinicians can use the system to make decisions and 4) accuracy.

This paper describes a novel, highly automated framework that enables clinicians to quickly and easily process pre-operative MR data, visualize scar and mechanical activation information, choose target locations and guide the CRT lead deployment. The system has been designed to use only the standard clinical X-ray fluoroscopy and MRI: short axis (SA) and long axis (LA) cine and LGE.

The proposed approach registers scar, anatomy and mechanical activation information to the same coordinate system and fuse this with fluoroscopic images, showing the CS anatomy. Furthermore, sophisticated scar metrics and visualizations are proposed to help clinicians identify potential targets for the LV CS lead deployment.

The system is demonstrated in an X-ray MR (XMR) facility where patients are scanned directly before the procedures. All preoperative data processing is performed in the time it takes to transfer the patient from the MR to the cath lab and start the procedure. This demonstrates the quality of the proposed systems and is testament to its speed, robustness and simple visualizations that enable the user to make fast decisions in the operating room. The accuracy of the system is evaluated on synthetic, phantom, volunteer and patient data.

II. Methods

This paper proposes a system for planning and guiding CRT procedures. An overview of the system is provided in Fig. 1. The system uses standard MRI SA and LA cine and LGE images to compute scar metrics and mechanical activation. The planning data is visualized in an intuitive approach that enables the clinician to select target regions which can be registered to intraoperative fluoroscopic images for guidance.

A. Myocardium Segmentation

The automatic segmentation of the myocardium [16] in SA and LA cine slices consists of five major steps: 1) landmark detection, 2) heart and blood pool localization, 3) deformable registration, 4) gray level analysis and 5) contour extraction.

The landmark detection uses a machine learning approach [17]. It was trained on landmarks including the mitral valve anchor points and apical point on LA views, the RV insertion points and RV lateral point on short axis images. The area around a landmark is represented by a bounding box with a given position, orientation, and scale. A marginal space search strategy is used to determine the position, orientation and scale of the bounding box given a new image. In addition, multiple

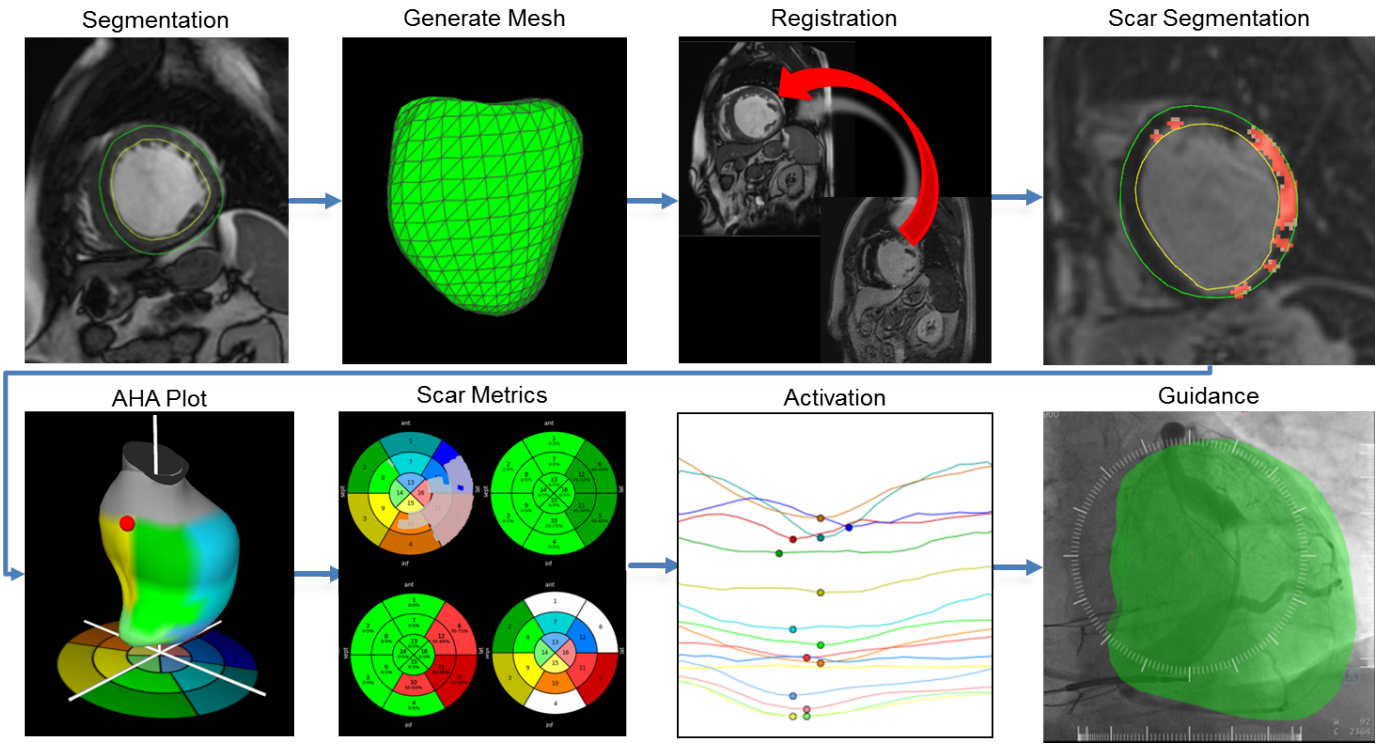

Fig. 1. An overview of the proposed CRT planning and guidance system from preoperative imaging to intraoperative guidance.

landmarks are combined in larger bounding boxes to define a larger context and increase the robustness of the detection.

In the heart and blood pool localization [18], the heart is detected by looking for the brightest moving object. A threshold is applied within that region to separate the blood pool from the myocardium region and locate a circular object that is most consistent through the slices.

A deformable registration algorithm [19] is used to compute the deformation fields between the first and any other frame in a slice by minimizing the local cross correlation between the two images. The algorithm uses an efficient scheme to update both the deformation and its inverse at each step of the gradient descent minimization in order to make the deformation field inverse consistent. In other words, $\phi_{ij} \circ \phi_{ij}^{-1} = \mathrm{id}$ and $\phi_{ij}^{-1} = \phi_{ji}$, where ϕ is the deformation field.

The gray level analysis consists of modeling the gray level distributions of the different regions (lungs, myocardium and blood). This step is then used to calculate a measure of probability for a pixel to belong to each of the regions. The Deriche filter edge detector is applied to the original images and the region probability images. Both are combined to calculate an edge cost for the endocardium and the epicardium.

The contour extraction within a slice uses the properties of the inverse consistent deformable registration. Each frame is examined one by one. For a frame p, the contour C_p is recovered in polar space using a shortest path algorithm and the edge cost function computed previously. The contours C_q in the other frames $q = 1, ..., P, q \neq p$ are generated using the deformation fields by $C_q(C_p) = \phi_{1q}(\phi_{1p}^{-1}(C_p))$. The energy of this contour series is computed based on the edge cost of each of the recovered contours. This same process is applied to all phases $p = 1, ..., P$ and the final segmentation is the one with the lowest energy. Contours are propagated between slices to initialize gray level analysis and contour recovery.

The segmentation of the myocardium in the long axis images employs a similar process. In the long axis images, the contours are not closed. However, mitral valve anchor points have been detected and the same algorithm is used to detect aortic valve anchor points. These landmarks are then used to specify the end points of the contours. In addition, the shortest path algorithm cannot be performed directly in a polar space because the contours are not round. Instead, a capped cylindrical space is defined.

B. Generating the LV Mesh

A 3D model of the LV can be directly derived from 2D SA and one or more LA cine segmentations. Due to the slice thickness (8 mm) and the gap between slices (2 mm) the model will be coarse and have visible steps that do not exist in the patient's anatomy, as shown in Fig. 2. A more realistic 3D model is generated by combining the LA segmentations and a 3D anatomical shape model of the heart [20].

The complexity of the LV anatomy is represented using an anatomical shape model created from a database of manually segmented MRI. The model includes the LV endocardium, LV epicardium and LV outflow tract. Each component of the model is a triangular mesh derived from the mean shape (an average model of all the annotations) of the anatomy.

The 3D anatomical model is aligned to the SA and LA cine images using the detected anatomical landmarks and the extracted contours. The contour-model alignment is performed on the individual slices. This has the added benefit of aligning

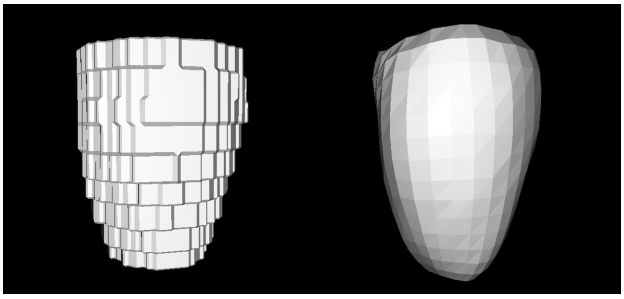

Fig. 2. Left, mesh derived from SA contours only. Right, mesh generated using the proposed method.

the SA slices to one another and the LA to the SA images. This results in a fully aligned SA stack that is registered with the LA images. To capture the true anatomical shape of the LV, the mean shape model is deformed by searching the SA and LA contours for each vertex of the model. The detected contours are constrained by projecting them onto a shape subspace obtained by the annotated dataset, which was constructed using principal component analysis. The result is a patient specific anatomical model of the LV shown in Fig 2 right.

C. 3D/3D MR Cine and LGE Image Registration

The MR cine and LGE images are registered to one another to allow anatomical and scar information to be analyzed in the same coordinate system.

The registration approach uses normalized mutual information (NMI) which is calculated between a reference image (anatomy) and a moving image (LGE) undergoing a rigid transformation. More formally, let I_1 be the reference image and I_2 be the moving image. A rigid transformation T is parameterized by a vector p composed of three rotation angles and a translation vector $\vec{t}$. The center of the coordinate system is temporarily shifted to the volumes geometric center during the registration process. Mutual information is used to measure the degree of dependency between the reference image I_1 and the transformed moving image $T(I_2)$. In order to reduce MI measurement sensitivity to the size of the overlap between I_1 and $T(I_2)$, the NMI [21] is used in the 3D/3D multi-modality registration implementation:

$$NMI(I_1, T(I_2)) = \frac{H(I_1) + H(T(I_2))}{H(I_1, T(I_2))} \tag{1}$$

where $H(I_1)$ and $H(T(I_2))$ are entropy of I_1 and $T(I_2)$ respectively, $H(I_1, T(I_2))$ is the joint entropy:

$$H(I_1) = -\sum_{i_1} p(i_1) log(p(i_1)) \tag{2}$$

$$H(T(I_2)) = -\sum_{i_2} p(i_2) log(p(i_2)) \tag{3}$$

$$H(I_1, T(I_2)) = -\sum_{i_1, i_2} p(i_1, i_2) log(p(i_1, i_2)) \tag{4}$$

where $p(i_1)$ and $p(i_2)$ are marginal probability density for I_1 and $T(I_2)$, and $p(i_1, i_2)$ is the joint probability density of I_1 and $T(I_2)$. The maximum of $NMI(I_1, T(I_2))$ is identified by a local hill climbing optimization method. This evaluates the cost for all neighboring vertices's of the current vertex in the parameter domain and takes the lowest cost vertex as the next location, iterating until the optimum is reached.

The computational efficiency and robustness is further improved by embedding the hill climbing algorithm in a coarse-to-fine multi-resolution strategy: 1) build multi-resolution pyramids composed of sub-sampled and low-pass filtered representations of the volumes; 2) apply the rigid registration on low-resolution images, then the results are used to initialize the alignment process at higher resolutions. This mechanism helps avoid local minima and speeds up the registration by recovering most of the transformation from smaller datasets. The sub-sampling mechanism used to build a coarser representation of a volume is not necessarily applied along all axes. It is designed to maximize the isotropy of the resulting volume. For instance, for volumes with large slice thickness the coarsening process will first take place in-plane. To avoid the influence of breathing motion from the chest wall, the objective function of registration is only calculated in a spherical region of interest encompassing the heart.

The LV mesh, cine and LGE images are visualized together in the registered coordinate system and the clinician is given the opportunity to manually adjust the 3D/3D registration. Following this, the user can perform a manual slice by slice registration of the LGE to the cine image by translating each slice in 2D. This accounts for any inaccuracies caused by patient movement between each LGE slice acquisition.

D. 3D 16 Segment AHA Model of the LV

The 16 segment AHA model is used to visualize the clinical metrics of scar and mechanical activation both in 2D and 3D. The model is generated by automatically dividing the LV into the standard 16 segments as shown in Fig. 3. The principal axis (PA) of the LV mesh, a line passing through the center of the surface and through the centers of curvature of all segments, is determined [11] by computing the first eigenvector of the positive definite matrix M, where

$$M = \frac{1}{n}(V - \overline{V})^T (V - \overline{V}) \tag{5}$$

where n is the number of vertices of the LV surface, V is an n by 3 matrix of 3D vertex points and $\overline{V}$ is the mean of all vertices. The valve is automatically detected and this region of the mesh is excluded from the segment calculation by extracting the subset of vertices that are up to a preset proportion. The subdivision method used firstly divides the LV into equal thirds perpendicular to its PA. This generates three circular sections; the basal, mid and apical. Both basal and mid circular sections are further divided into six segments using two anatomical landmarks: the insertion points connecting the RV and LV wall. The apical section is divided into four segments of 90° each.

E. Scar Segmentation

The scar and border zone segmentation in the LGE image is semi automated and exploits recommended tissue-pixel inten-

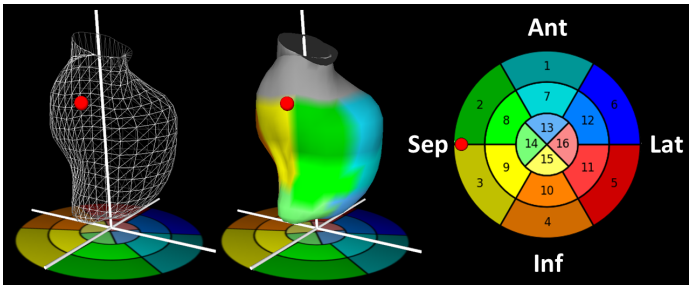

Fig. 3. Left, 3D LV above the 2D AHA plot. Middle, 3D LV divided into 16 AHA segments. Right, 2D AHA plot. Red dot is RV insertion point.

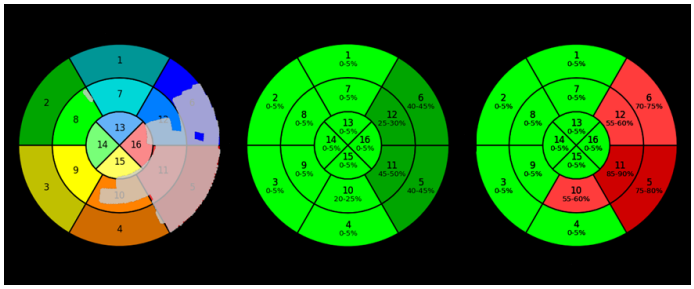

Fig. 5. Left, scar distribution. Middle, scar burden. Right, scar transmurality.

sity parameters from the literature. Pixels in the myocardium with gray levels that are three or more standard deviations away from the mean healthy tissue are good candidates for scar tissue and between two and three standard deviations away are likely to be border zone [22]. The myocardium cannot be accurately directly derived in the LGE image due to the similarity between scar and the blood pool. The epicardial and endocardial meshes from the cine image are transformed to the LGE image space and projected into the LGE slices as shown in Fig. 4 left.

The clinician is required to select a small area of healthy tissue in the myocardium. Statistics are computed from the sampled pixel and thresholds are chosen for border zone and scar tissue Fig. 4 middle and right. The clinician is presented with the histogram of the myocardium region and the location of the two thresholds. The user is free to adjust the threshold to refine the segmentation. Only scar tissue is used for planning and guidance and border zone tissue is ignored. The result is a set of SA binary scar masks and a 3D scar mesh.

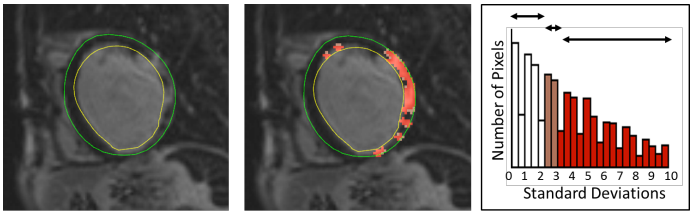

Fig. 4. Scar Segmentation. Left, the endocardial (yellow) and epicardial (green) contours segmented from cine images overlaid on the SA LGE image. Middle, red semi transparent pixels indicate scars. Right, intensity histogram, white - healthy tissue, yellow - border zone and red - scar tissue.

F. Scar Distribution

Scar distribution (shown in Fig. 5) displays the location of scar on the 2D AHA 16 segment plot. The 3D scar mesh is mapped to a 2D plot by representing the 3D scar location in polar coordinates on the LV surface. The angle is defined by the RV direction in a plane perpendicular to the PA. The radius is defined as the distance from the apex along the PA as a proportion of the height of the segmented region. It is important to note that the scar distribution does not account for the thickness or position of scar in the myocardial wall. To fully understand scar, more comprehensive visualizations are required to see the burden and transmurality.

G. Scar Burden

Scar burden is the percentage of scar tissue in the myocardium. It is averaged in each AHA segment to make it intuitive for clinicians to interpret. It is computed using the SA segmented scar mask. Each voxel of the mask is projected into the coordinate system of the 2D 16 segment AHA heart model and assigned a color (Fig. 6). The segmented image is used to calculate the percentage of scar in each of the 16 segments as shown in Fig. 5 and the total scar burden.

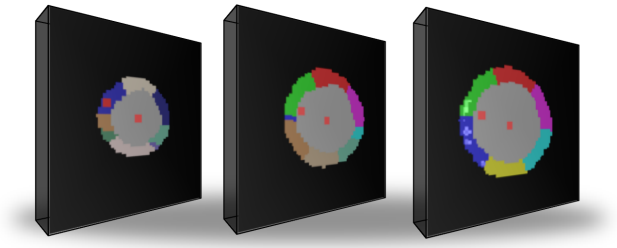

Fig. 6. 16 segment AHA color coded slices of the LV. The scar is shown in semi-transparent white. The red dots on the images illustrate the centre of the scar slices and the direction of the RV.

H. Scar Transmurality

Fully transmural scar extends the entire thickness of the myocardial wall from the endocardial to the epicardial surface. Fully transmural scar tissue is not conducive to good CRT response. However, the wall may only be partially scarred with a combination of healthy and damaged tissue. If the scar is on the opposite side of the wall to the lead, a feasible location may be found. It is challenging to visualize the extent of scarring, as demonstrated by a contrived example in Fig. 7. In this work, scar transmurality is visualized in 2D with quantitative statistics (Fig. 5) and in 3D with interactive scar layers (Fig. 7).

2D scar transmurality is visualized in the 16 segment AHA plot. Each segment in this 16-segment model was further subdivided into 10 smaller regions. A region represents a small section of the myocardium around a radial line. Within each region, the transmurality was computed using a ray tracing technique. A ray was traced from the center of the left ventricle to the epicardium, in each region. The extent of scar along each ray was calculated and this determined the transmural extent of scar in every region. The median transmurality is computed for each segment in the 16-segment model, giving a transmurality percentage and color coded as shown in Fig. 5.

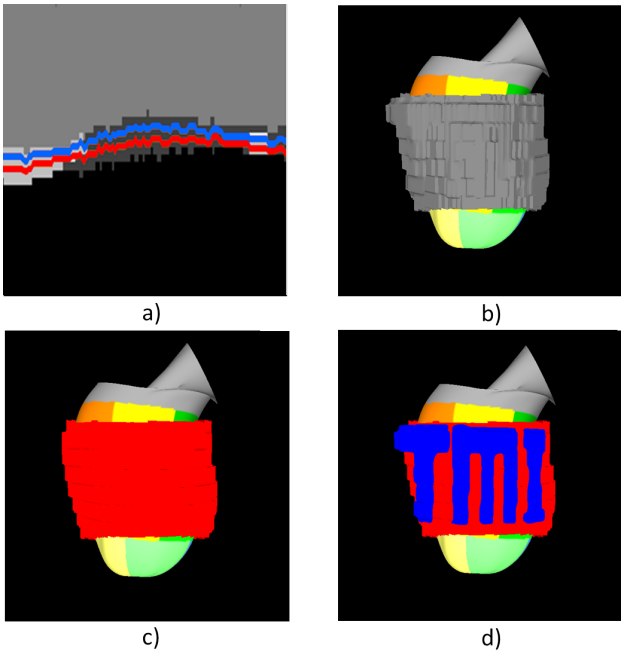

Fig. 7. Illustration of scar peeling. a) The myocardium in polar coordinate system showing scar (light gray), healthy tissue (dark gray) and blood pool (black). The scar layers are shown in blue and red. b) All scar visualized as a gray mesh overlaid on the endocardium to illustrate the challenge of interpreting transmurality. c) One scar layer showing endocardial scar (red). d) Two scar layers showing endocardial (red) and epicardial (blue) scar.

The scar transmurality is additionally visualized in 3D using interactive layers [23], shown in (Fig. 7). Three layers are used from epicardial to mid-myocardial to endocardial which corresponds to the clinical descriptions of scar. This provides an intuitive visualization that reveals the extent of the tissue damage. The binary mask of the segmented scar in the SA LGE image and contours delineating the endocardial and epicardial surface are converted to a polar coordinate space. In the transformed space, the contours are of equal length and are approximately parallel to each other. The space between the contours is divided into three equal sections to create the scar layers. The layers are transformed back to the binary mask image coordinate system and the marching cubes algorithm is used to create three scar layers.

I. Mechanical Activation and Dyssynchrony Indices

The automatically segmented SA endocardial and epicardial contours are equally divided into three layers representing apex, mid and basal. These contours are further divided into segments using the angle relative to the RV direction in each slice (Fig. 8). The area of each of the segments within the slice is then calculated. Using the AHA 16 segment areas and the slice thicknesses, the volume of each of the segments throughout the cardiac cycle is computed in millilitres using Equation 6,

$$EV = |area_{segment}| \times (slice\ thickness) \quad (6)$$

where EV corresponds to the endocardial volume. A series of time-volume curves representing the change in volume are generated (Fig. 8). The time to maximum contraction is calculated for each segment and is expressed as a percentage of the total cardiac cycle. Consequently, the most delayed segment, considered as the optimal pacing segment that will achieve the maximum resynchronization effect, is identified. The approach is well suited to in-slice dyssynchrony which is commonly observed in CRT patients.

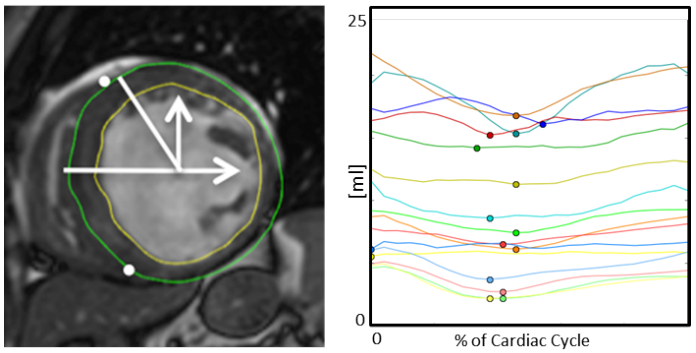

Fig. 8. Left, an example of a basal contour segment division. The two anatomical landmarks (white dots) are the RV insertion points. Right, LV mechanical activation curves for a patient with dyssynchrony.

LV mechanical dyssynchrony indices based on volumetric analysis are extracted. These include systolic dyssynchrony index (SDI), ejection fraction (EF), stroke volume (SV), end-diastolic volume (EDV) and end-systolic volume (ESV). EDV is the amount of blood in the ventricle immediately after ventricular diastole and just before it contracts again. ESV refers to the blood volume left in the ventricle immediately after contraction, and is the lowest volume of blood in the ventricle at any point in the cardiac cycle. SV is determined by $EDV - ESV$. EF is the fraction of blood ejected by the left ventricle (LV) during the contraction or ejection phase of the cardiac cycle (systole), $\frac{SV}{EDV} \cdot 100$. The SDI is the standard deviation of the regional times to maximum contraction and is expressed as a percentage of the cardiac cycle.

J. Planning Target Selection

Following the processing of the preoperative MRI and the computation of scar and mechanical activation information the clinical team is presented with the intuitive and simple visualization described above. The team is able to interact with the visualization to further compare target segments and identify the most appropriate areas for LV lead deployment. The platform allows multiple target segments to be selected in the 2D AHA plot. A 3D mesh showing the target segments is automatically generated from the 2D selected segments. Both the 2D and 3D visualization of the target segments are made available during the procedure.

K. Guidance

X-ray fluoroscopy is used during the procedure to deploy the device leads. A registration is performed to align the pre-operative MRI to the intra-operative X-ray images to overlay planning data on the X-ray. Two manual registration workflows

were investigated: 1) fiducial based and 2) mesh based. In both approaches, two X-ray images are acquired with contrast injection of the CS (either bi-plane or sequential mono-plane). These images are best captured at end expiration and mid diastolic phase although this is not always possible.

Fiducial based registration: XMR facilities where the MR image is acquired immediately before the intervention enable fiducials to be placed on the patient's chest, as shown in Fig. 9. The fiducials can be difficult to locate in the MRI slices and therefore, an additional 3D MRI was acquired. The MRI is aligned to the X-ray by matching the iso-center of the C-Arm to the image center. The volume rendered MR is projected onto the X-ray and the two images are manually aligned (six degrees of freedom) to one another.

Mesh based registration: This more general approach does not require an XMR facility or fiducials however, it is more challenging and time consuming. The MR is first aligned to the C-Arm iso-center. The LV epicardial mesh is aligned to the X-ray images using the clinician's anatomical knowledge usually using weak landmarks, such as the heart shadow and the contrast injected CS (Fig. 9).

During guidance, the following 3D meshes can be overlaid on the X-ray: scar, target segments, 3D 16 segment AHA. Additionally, all planning information is made available.

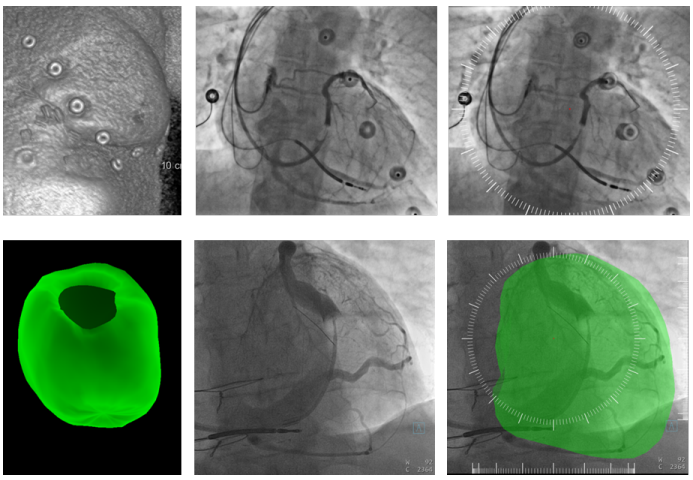

Fig. 9. MR to X-ray registration. Top - fiducial registration, left - fiducials in MRI, middle - fiducials in X-ray and right - registered fiducials with registration wheel. Bottom - mesh based registration, left - MRI derived LV mesh, middle - X-ray image showing constrasted CS and heart shadow, right - registered mesh with registration wheel.

III. Results

The proposed system is quantitatively and qualitatively validated on phantom, simulated, healthy volunteer and patient data. Parts of the system have been previously validated on different pathologies. In this paper, the proposed system is validated for planning and guiding CRT procedures.

A. Phantom Data

A 3D phantom was created for validation. The LV of a patient was segmented from MRI and the endocardial and epicardial meshes were combined with additional supports and 3D printed. The printed LV was injected with silicon between the endocardium and epicardium to simulate scar tissue and encased in a box with fiducial markers on the walls. Automatic segmentation was not evaluated on the phantom, because it relies on landmarks outside the LV and MR imaging of plastic and silicon does not directly map to human tissue.

B. Anatomy Segmentation

The automatic LV segmentation of the SA cine images is quantitatively evaluated on 14 CRT patients. Ground truth contours of the endocardium and epicardium were annotated by an expert user. Slices near the valve and at the apex are excluded as these are not of interest for CRT. Fig. 10 shows the average Dice coefficient for each procedure. The Dice coefficient is computed for each cine slice using the myocardial tissue which is defined as the area between the endocardium and epicardium contours. The average Dice coefficient for all slices in all procedures was 88.0 % indicating the clinical practicality of the approach. Errors are attributed to low quality images caused by motion artifacts. A comprehensive evaluation on a variety of pathologies is provided in [16].

During the CRT procedure, the clinician can amend or correct the automatic segmentation. To further demonstrate the clinical applicability, the automatic segmentation was compared to the amended segmentation. The average Dice coefficient was 97.0 %. In eight patients the segmentation was not amended and in five cases only minor changes were made. Larger edits were made in only a single case.

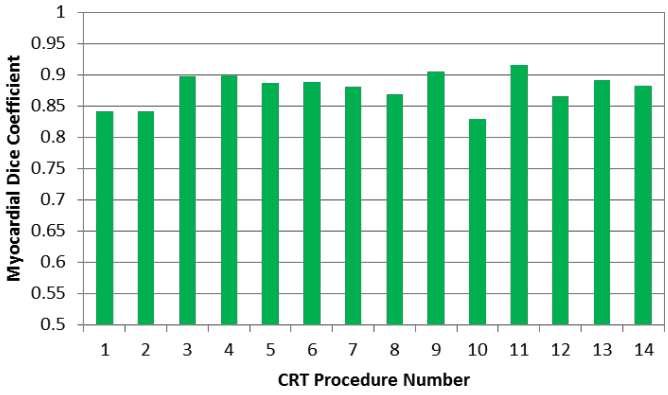

Fig. 10. Quantitative SA LV segmentation evaluation. Myocardial tissue Dice coefficient for automatic segmentation and ground truth annotations.

C. 3D/3D Registration Cine to LGE

The automatic 3D/3D registration of SA cine to SA LGE images is evaluated on 14 CRT cases. Ground truth registrations were obtained by an expert user manually aligning the two images. The root mean square (RMS) error for translation was 2.0 mm and standard deviation (SD) of 1.4 mm. More detailed analysis is provided in Table I. These errors are considered small in the context of the MRI LGE resolution (X = 1.77 mm, Y = 1.77 mm, Slice thickness 8 mm).

During the procedure, the clinician can manually correct the 3D/3D registration and align the LGE slices in 2D. Small

TABLE I
3D/3D REGISTRATION ERROR: MR CINE TO MR LGE

	Average	Standard Deviation	Min	Max
3D Registration Error (mm)	2.05	1.36	0.11	5.15
X Axis Error (mm)	0.89	1.02	0.04	4.04
Y Axis Error (mm)	1.13	0.98	0.07	3.60
Z Axis Error (mm)	1.05	0.97	0.00	2.71

manual adjustments were made to the 3D/3D registration (mean 1.8 mm) and the 2D LGE slices (mean 4.8 mm).

D. Scar Burden and Distribution

Scar burden and distribution are validated on phantom data and healthy volunteer data with simulated scar. A phantom experiment was performed to validate the total scar burden. Short and long axis, LGE and cine images were captured and processed through the platform. The contours and scar were manually segmented and the total scar burden was computed as 30 % compared to 36 % ground truth. The difference is attributed to manual annotation and 8 mm slice thickness.

The visualization of scar burden and distribution in the 2D AHA plots are validated using a healthy volunteer's MRI, augmented with simulated scar. Two datasets were created by manually drawing scar on the anterior and inferior halves of the LV. The results are shown in Fig. 11. It can be clearly seen in the scar distribution visualizations (Fig. 11 left) that the scar (gray area) location corresponds to the anterior and inferior anatomy. The scar burden (Fig. 11 right) is accurately computed. The simulated scar was added with 100 % transmurality leading to 100 % burden in areas with 100 % distribution. Small inaccuracies can occur around the apex due to the resolution of the MRI.

E. Mechanical Activation

The mechanical activation is validated on healthy volunteer and simulated data shown in Fig. 12. The mechanical activation is computed from sets of 2D contours that outline the myocardium in each cine slice and time frame. The simulated data used a set of contours from a healthy volunteer with synchronous activation and manipulated these contours to simulate delayed activation in specific regions. To simulate a delay of 20 % of the cardiac cycle in a region (e.g. septal), the motion of the part of the contour in that region was paused for the first 20 % of the cycle. This is equivalent to a phase shift in time. This created new myocardium contours with regions of delayed activation. Four experiments were performed with delayed activation in the septal and lateral regions with delays of 20 % and 40 %.

The results for septal delay are shown in Fig. 12 c) and e). The minimum points of the yellow and green lines - corresponding to the septal areas - are delayed. Similar results are shown in Fig. 12 d) and f) for the blue and red lateral lines. In both septal and lateral, all minimum points are correctly computed to within 4 % of the simulated delay which corresponds to one time frame.

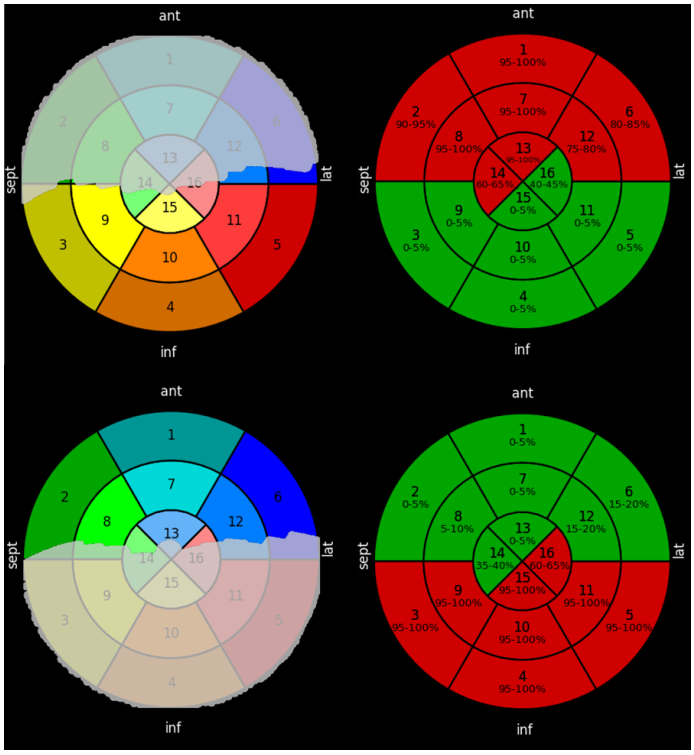

Fig. 11. Scar distribution and burden on the anterior and inferior walls.

F. Guidance

Image guidance is evaluated on phantom and clinical data. Using X-ray the phantom's endocardium, epicardium, scar and fiducials are visible (Fig. 13). The epicardial mesh was registered to the X-ray using the fiducials and the epicardial outline. Qualitative evaluation is provided in Fig. 13. Overlays are shown for two X-ray angulations where a) and d) show the manually annotated silicon scar and b) and e) show the silicon scar segmented in the MRI. The overlay is quantitatively evaluated using the Dice coefficient of the manually annotated and projected anatomy. The results for the epicardium was mean 92.0 %, SD 3.4 % and for scar it was 87.9 %, SD 4.6 %. Differences in the ground truth and overlay are due to the MRI resolution and inaccuracies in the manual segmentation.

Fig. 14 f) and h) qualitatively illustrate the overlay on clinical data. Quantitative validation was performed by manually annotating the heart shadow in the X-ray image and comparing it to the overlaid epicardial mesh. The average Dice coefficient was 87.6 % (SD 3.6 %). This indicates the overlay accuracy; however, annotating the LV shadow in X-ray is extremely challenging as it is only partially visible.

G. CRT Procedure

14 patients were treated with the proposed platform. Complementary to this technical paper, a clinical evaluation was performed to assess patient outcome [24]. An example is shown in Fig. 14 of a patient treated in an XMR facility with the preoperative image acquired directly before the procedure.

The mechanical activation and scar metrics are shown in Fig. 14 a-d). It can be clearly seen that there is scar on the

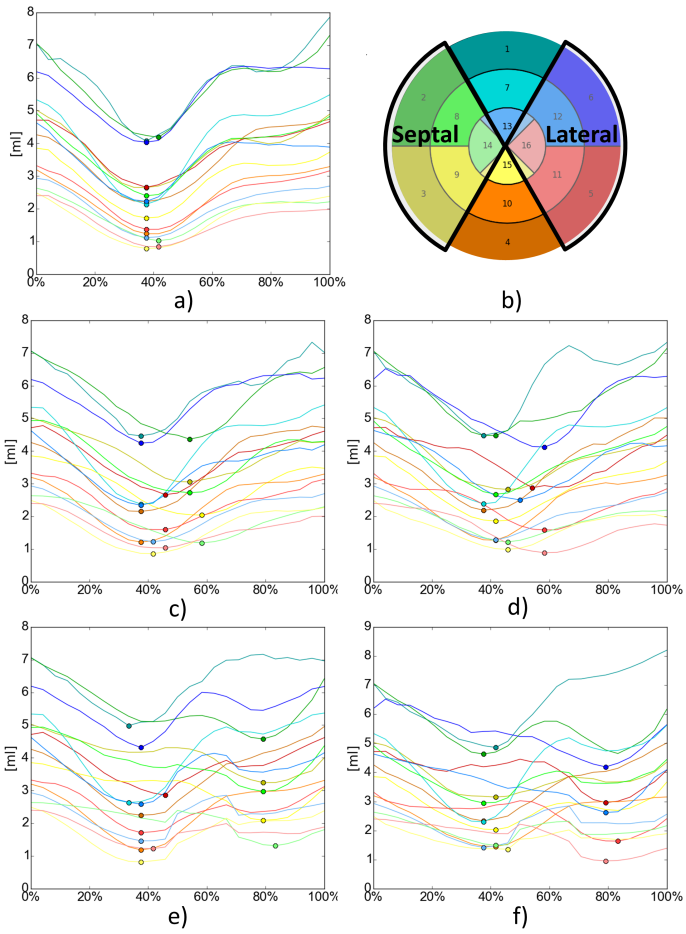

Fig. 12. Mechanical activation. a) Synchronous healthy volunteer. b) Septal and lateral regions. c-f) simulated delay. c) septal 20 % d) lateral 20 %, e) septal 40 % and f) lateral 40 %.

lateral wall. This is generally a good location for the LV lead; however, for this patient it was possible to target alternative segments to increase the chance of response. The clinicians identified segments one, four and six as targets. Segment six was chosen as a potential target despite being partially scarred. This is due to the late activation of the sector. The selected target areas are shown in Fig. 14 e) and i) and overlaid on the X-ray to guide the lead deployment.

During the planning stage, it was observed that the clinical team followed a pattern for identifying potential target locations. 1) focus on lateral, inferior, anterior and non apical segments. 2) evaluate scar by examining (in order), distribution, burden and transmurality. 3) compare mechanical activation.

Guidance was used during LV lead deployment. The clinical team overlaid the target locations, the raw scar mesh and AHA 3D mesh. The registration was manually updated during the procedure to account for minor patient movements.

IV. Conclusions

This paper describes a comprehensive planning and guidance system for CRT. The novel system uses standard clinical MRI to quantify scar and mechanical activation. This information assists clinicians to identify target areas for the

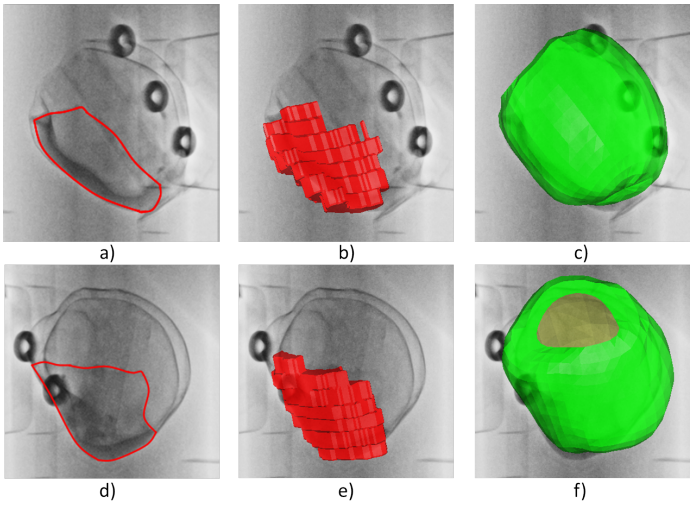

Fig. 13. Guidance platform. Phantom MRI data overlaid on two X-ray images representing LAO and RAO. a) and d) X-ray images with annotated silicon scar outlined in red. b) and e) MRI segmented scar mesh overlaid on X-ray. c) and f) the epicardial mesh overlaid on X-ray.

deployment of the LV lead. The preoperative planning data is overlaid on X-ray images to guide the procedure and improve the likelihood of a patient responding.

The proposed system is highly automated and complements the current clinical workflow by registering all data to a single coordinate system and providing intuitive visualization. It has been validated on synthetic, phantom, volunteer and patient data. The practical, clinical application has been shown on 14 CRT implants. The platform's main limitation is the manual registration of MR to X-ray which is highly user dependent and challenging, due to lack of cross modality landmarks. Future work will focus on incorporate more automated registration.

The plaform has potential for significant impact on the medical imaging and the clinical communities. It is flexible and extensible, it can easily incorporate other clinical information (e.g. wall thickness or electrical activation). Additionally, it is being used to explore new applications in wireless endocardial pacing and congenital cardiac procedures.

V. Acknowledgements and Disclaimer.

The authors would like to thank Tanja Kurzendorfer, Benjamin J. Sieniewicz, Justin Gould, Simon Claridge, Tom Jackson, Indraneel Borgohain, Bogdan Georgescu, Craig Buckley and Bernhard Fahn for their help and support. The authors are grateful for the support from the Innovate UK grant 32684-234174. The research was supported by the National Institute for Health Research (NIHR) Biomedical Research Centre based at Guys and St Thomas NHS Foundation Trust and Kings College London. The views expressed are those of the authors and not necessarily those of the NHS, NIHR or the Department of Health. Concepts and information presented are based on research and are not commercially available.

References

[1] D. Mozaffarian, E. J. Benjamin, A. S. Go, D. K. Arnett, M. J. Blaha, M. Cushman, S. de Ferranti, J.-P. Desprs, H. J. Fullerton, V. J. Howard,

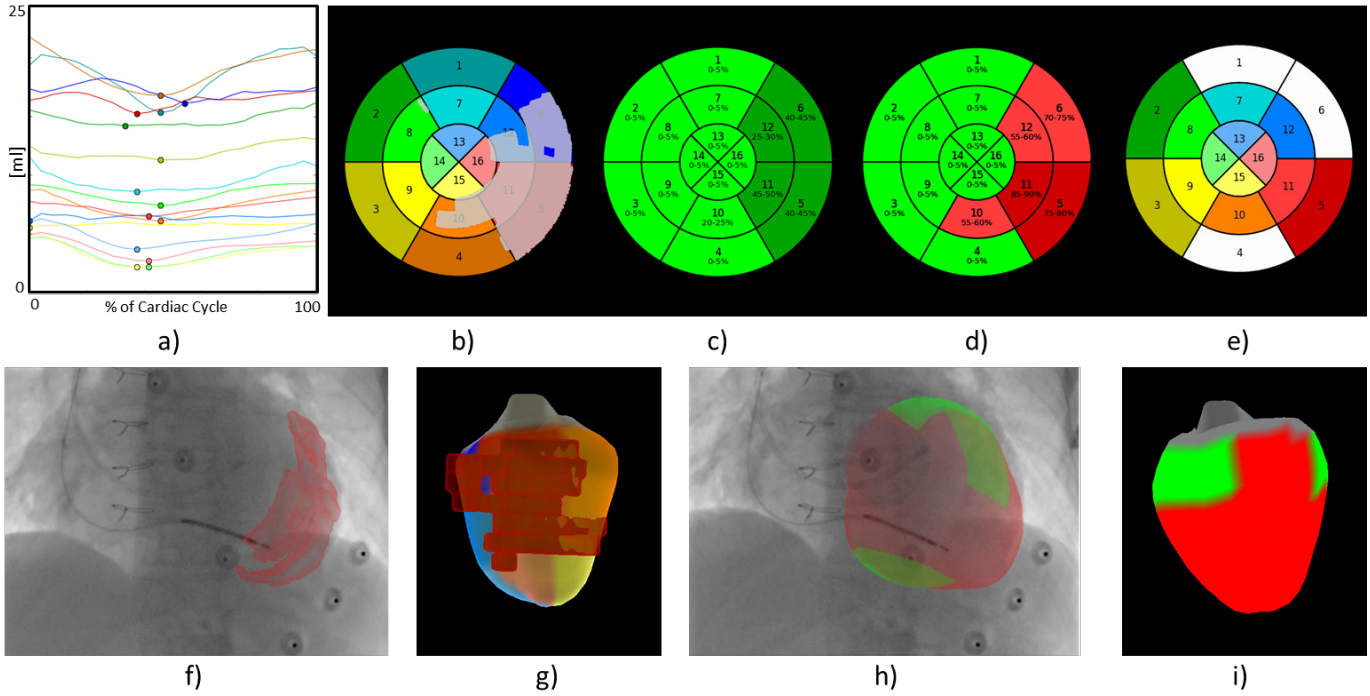

Fig. 14. Planning and Guidance Platform for a one patient. a) Mechanical activation, b) scar distribution, c) scar burden, d) scar transmurality, e) selected target segments (white), f) scar mesh overlaid on X-ray, g) 3D scar mesh and 16 segmented 3D endocardial mesh, h) target segments overlaid on X-ray (green) and i) target segments in 3D. Note, segment six is selected as a potential target segment even though it contains scar.

M. D. Huffman, S. E. Judd, B. M. Kissela, D. T. Lackland, J. H. Lichtman, L. D. Lisabeth, S. Liu, R. H. Mackey, D. B. Matchar, D. K. McGuire, E. R. Mohler, C. S. Moy, P. Muntner, M. E. Mussolino, K. Nasir, R. W. Neumar, G. Nichol, L. Palaniappan, D. K. Pandey, M. J. Reeves, C. J. Rodriguez, P. D. Sorlie, J. Stein, A. Towfighi, T. N. Turan, S. S. Virani, J. Z. Willey, D. Woo, R. W. Yeh, and M. B. Turner, "Heart Disease and Stroke Statistics 2015 Update: A Report From the American Heart Association," *Circulation*, vol. 131, no. 4, pp. e29–e322, Jan. 2015.

[2] J.-C. Daubert, L. Saxon, P. B. Adamson, A. Auricchio, R. D. Berger, J. F. Beshai, O. Breithard, M. Brignole, J. Cleland, D. B. DeLurgio *et al.*, "2012 ehra/hrs expert consensus statement on cardiac resynchronization therapy in heart failure: implant and follow-up recommendations and management," *Europace*, vol. 14, no. 9, pp. 1236–1286, 2012.

[3] C. Thebault, E. Donal, C. Meunier, R. Gervais, B. Gerritse, M. R. Gold, W. T. Abraham, C. Linde, J.-C. Daubert, R. S. Group, and others, "Sites of left and right ventricular lead implantation and response to cardiac resynchronization therapy observations from the REVERSE trial," *European heart journal*, vol. 33, no. 21, pp. 2662–2671, 2012.

[4] J. P. Singh, H. U. Klein, D. T. Huang, S. Reek, M. Kuniss, A. Quesada, A. Barsheshet, D. Cannom, I. Goldenberg, S. McNitt, and others, "Left ventricular lead position and clinical outcome in the multicenter automatic defibrillator implantation trialcardiac resynchronization therapy (MADIT-CRT) trial," *Circulation*, vol. 123, no. 11, pp. 1159–1166, 2011.

[5] E. K. Heist, D. Fan, T. Mela, D. Arzola-Castaner, V. Y. Reddy, M. Mansour, M. H. Picard, J. N. Ruskin, and J. P. Singh, "Radiographic left ventricular right ventricular interlead distance predicts the acute hemodynamic response to cardiac resynchronization therapy," *The American journal of cardiology*, vol. 96, no. 5, pp. 685–690, 2005.

[6] C. Ypenburg, M. J. Schalij, G. B. Bleeker, P. Steendijk, E. Boersma, P. Dibbets-Schneider, M. P. Stokkel, E. E. van der Wall, and J. J. Bax, "Impact of viability and scar tissue on response to cardiac resynchronization therapy in ischaemic heart failure patients," *European heart journal*, vol. 28, no. 1, pp. 33–41, 2007.

[7] F. Leyva, P. W. Foley, S. Chalil, K. Ratib, R. E. Smith, F. Prinzen, and A. Auricchio, "Cardiac resynchronization therapy guided by late gadolinium-enhancement cardiovascular magnetic resonance," *J Cardiovasc Magn Reson*, vol. 13, no. 1, pp. 29–35, 2011.

[8] C. Ypenburg, R. J. van Bommel, V. Delgado, S. A. Mollema, G. B. Bleeker, E. Boersma, M. J. Schalij, and J. J. Bax, "Optimal left ventricular lead position predicts reverse remodeling and survival after cardiac resynchronization therapy," *Journal of the American College of Cardiology*, vol. 52, no. 17, pp. 1402–1409, 2008.

[9] R. T. Murphy, G. Sigurdsson, S. Mulamalla, D. Agler, Z. B. Popovic, R. C. Starling, B. L. Wilkoff, J. D. Thomas, and R. A. Grimm, "Tissue synchronization imaging and optimal left ventricular pacing site in cardiac resynchronization therapy," *The American journal of cardiology*, vol. 97, no. 11, pp. 1615–1621, 2006.

[10] Y. L. Ma, A. K. Shetty, S. Duckett, P. Etyngier, G. Gijsbers, R. Bullens, T. Schaeffter, R. Razavi, C. A. Rinaldi, and K. S. Rhode, "An integrated platform for image-guided cardiac resynchronization therapy," *Physics in Medicine and Biology*, vol. 57, no. 10, pp. 2953–2968, May 2012.

[11] Y. Ma, S. Duckett, P. Chinchapatnam, A. Shetty, C. A. Rinaldi, T. Schaeffter, and K. S. Rhode, "Image and physiological data fusion for guidance and modelling of cardiac resynchronization therapy procedures," in *Statistical Atlases and Computational Models of the Heart*. Springer, 2010, pp. 105–113.

[12] W. Zhou, X. Hou, M. Piccinelli, X. Tang, L. Tang, K. Cao, E. V. Garcia, J. Zou, and J. Chen, "3d fusion of LV venous anatomy on fluoroscopy venograms with epicardial surface on SPECT myocardial perfusion images for guiding CRT LV lead placement," *JACC: Cardiovascular Imaging*, vol. 7, no. 12, pp. 1239–1248, 2014.

[13] F. Tavard, A. Simon, C. Leclercq, E. Donal, A. Hernndez, M. Garreau, and others, "Multimodal registration and data fusion for cardiac resynchronization therapy optimization," *Medical Imaging, IEEE Transactions on*, vol. 33, no. 6, pp. 1363–1372, 2014.

[14] S. Bruge, A. Simon, M. Lederlin, J. Betancur, A. Hernandez, E. Donal, C. Leclercq, and M. Garreau, "Multi-modal data fusion for Cardiac Resynchronization Therapy planning and assistance," in *2015 37th Annual International Conference of the IEEE Engineering in Medicine and Biology Society (EMBC)*, Aug. 2015, pp. 2391–2394.

[15] D. Toth, M. Panayiotou, A. Brost, J. M. Behar, C. A. Rinaldi, K. S. Rhode, and P. Mountney, "Registration with adjacent anatomical structures for cardiac resynchronization therapy guidance," in *International Workshop on Statistical Atlases and Computational Models of the Heart*. Springer, 2016, pp. 127–134.

[16] M.-P. Jolly, C. Guetter, X. Lu, H. Xue, and J. Guehring, "Automatic segmentation of the myocardium in cine mr images using deformable registration," in *Proc. Workshop Statistical Atlases and Computational*

Models of the Heart: Imaging and Modelling Challenges, 2011.

[17] X. Lu, B. Georgescu, M.-P. Jolly, J. Guehring, A. Young, B. Cowan, A. Littmann, and D. Comaniciu, "Cardiac anchoring in mri through context modeling," in *Proc. Medical Image Computing and Computer-Assisted Intervention*, 2010.

[18] M.-P. Jolly, "Automatic recovery of the left ventricular blood pool in cardiac cine mr images," in *Proc. Medical Image Computing and Computer-Assisted Intervention*, 2008.

[19] C. Guetter, H. Xue, C. Chefdhotel, and J. Guehring, "Efficient symmetric and inverse-consistent deformable registration through interleaved optimization," in *Proc. Int. Symp. Biomedical Imaging: From Nano to Macro*, 2011.

[20] X. Lu, Y. Wang, B. Georgescu, A. Littman, and D. Comaniciu, "Automatic delineation of left and right ventricles in cardiac mri sequences using a joint ventricular model," in *International Conference on Functional Imaging and Modeling of the Heart*. Springer, 2011, pp. 250–258.

[21] C. Studholme, D. L. Hill, and D. J. Hawkes, "An overlap invariant entropy measure of 3d medical image alignment," *Pattern recognition*, vol. 32, no. 1, pp. 71–86, 1999.

[22] A. T. Yan, A. J. Shayne, K. A. Brown, S. N. Gupta, C. W. Chan, T. M. Luu, M. F. Di Carli, H. G. Reynolds, W. G. Stevenson, and R. Y. Kwong, "Characterization of the peri-infarct zone by contrast-enhanced cardiac magnetic resonance imaging is a powerful predictor of postmyocardial infarction mortality," *Circulation*, 2006.

[23] S. Reiml, D. Toth, M. Panayiotou, B. Fahn, R. Karim, J. M. Behar, C. A. Rinaldi, R. Razavi, K. S. Rhode, A. Brost, and P. Mountney, "Interactive visualization for scar transmurality in cardiac resynchronization therapy," pp. 97 862S–97 862S–8, 2016.

[24] J. Behar, P. Mountney, D. Toth, S. Reiml, M. Panayiotou, A. Brost, B. Fahn, R. Karim, S. Claridge, T. Jackson, B. Sieniewicz, N. Patel, M. ONeill, R. Razavi, K. Rhode, and C. A. Rinaldi, "Real-Time X-MRI-Guided Left Ventricular Lead Implantation for Targeted Delivery of Cardiac Resynchronization Therapy," *JACC: Clinical Electrophysiology*, Apr. 2017.